Application of Bayesian Optimization for High-Performance TiO$_x$/SiO$_y$/c-Si Passivating Contact

Shinsuke Miyagawa[1]*, Kazuhiro Gotoh[1], Kentaro Kutsukake[2], Yasuyoshi Kurokawa[1] and Noritaka Usami[1]*

[1]*Graduate School of Engineering, Nagoya University, Furo-cho, Chikusa-ku, Nagoya, 464-8603, Japan*

[2]*Center for Advanced Intelligence Project, RIKEN, Tokyo 103-0027, Japan*

E-mail: miyagawa.shinsuke@icloud.com, usa@material.nagoya-u.ac.jp

Highlights

・Bayesian optimization was applied to the practical fabrication process of titanium oxide/silicon oxide/crystalline silicon passivating contact.

・Bayesian optimization using multiple sets of samples with different pre-deposition treatments could permit optimization of deposition and post-deposition processes while choosing superior pre-deposition treatment.

・The optimization of the carrier selectivity estimated by independent measurements of the saturation current density and contact resistance was achieved by Bayesian optimization of only 12 cycles and 10 initial random experiments.

Abstract

We report on the application of Bayesian optimization (BO), which could accelerate the time-intensive process optimization of many parameters, to fabrication of the high-performance titanium oxide/silicon oxide/crystalline silicon passivating contact. The process contains pre-deposition treatment to form SiO_y interlayer, atomic layer deposition (ALD) of TiO_x, and hydrogen plasma treatment (HPT) as post-process. We attempted to optimize seven parameters for ALD and HPT by dealing with samples treated by three kinds of chemical solutions in the same batch. This permits to perform BO for each structure at the same time and determine the superior pre-deposition treatment. Consequently, carrier selectivity S_{10} estimated by independent measurements of the saturation current density and contact resistance was significantly improved by BO of only 12 cycles and 10 initial random experiments. These results certify that BO could efficiently provide experimental conditions in multidimensional parameter space although we need to consider the impact of the metallization process on the passivation performance.

1. Introduction

Silicon heterojunction (SHJ) solar cells have accomplished high power conversion efficiency (PCE) around 25% [1-4]. In SHJ solar cells, passivating contacts (PCs) play a key role in the efficient separating and transporting of photo-generated carriers in crystalline silicon (c-Si). Furthermore, PCs require the suppression of carrier recombination at the PCs/c-Si heterointerface for reducing the carrier recombination loss of solar cells. In PCs, hydrogenated amorphous Si (a-Si:H) is known as an excellent PC material due to its great passivation performance [1-4]. However, the bandgap energy (E_g) of a-Si:H is relatively low (~1.7 eV), resulting in decreasing in the short current density owing to parasitic absorption in a-Si:H layer [5-7]. In this regard, alternative materials to a-Si:H is crucial for further improvement in SHJ solar cells.

Recently, there are a lot of studies of transition metal oxides to utilize for PCs. Molybdenum oxide [8-11], vanadium oxide [8,12] and tungsten oxide [8,13] are gathering attention for hole-selective contacts (HSCs). On the other hand, titanium oxide (TiO_x) is intensively studied as electron-selective contacts (ESCs) for SHJ solar cells [14-17]. The TiO_x/c-Si heterostructure forms the small conduction band offset (< 0.05 eV) and large valence band offset (> 2.0 eV), and thus electrons can be transported whereas holes are repelled [14,18,19]. Moreover, the parasitic absorption of TiO_x is negligible due to the wider E_g of 3.3 eV than that of a-Si:H [20,21].

However, the passivation performance of TiO_x is inferior to that of a-Si:H. Many studies have been devoted to improving the passivation performance of TiO_x and the following process are developed to realize high passivation performance [22-34]. Firstly, TiO_x should be prepared by atomic layer deposition (ALD) for good passivation

performance due to the low deposition damage and large-area uniformity [22-24]. Furthermore, ALD provides precise film thickness control to fabricate a few nm TiO_x film which suppresses the increase of the series resistance due to TiO_x itself. Secondly, the inserting silicon oxide (SiO_y) interlayer between TiO_x and c-Si has been reported to improve the passivation performance [25-29]. It is considered that this improvement is attributed to the formation of Si-O-Ti bonds by the diffusion of Ti and O atoms from TiO_x to SiO_y [27]. Finally, the thermal process after TiO_x deposition is important to enhance the passivation performance. There are many reports that the ALD-TiO_x layer can provide a high passivation performance after post-annealing [22-30]. These reports suggest that the improved passivation performance can be caused by an O-terminated c-Si surface [29]. In recent years, hydrogen plasma treatment (HPT) is found to improve the performance of TiO_x/c-Si heterostructure [31-34]. HPT can supply hydrogen to the TiO_x/c-Si interface and thus interfacial dangling bonds are terminated by hydrogen atoms [32]. Moreover, HPT can be performed at a lower temperature than annealing, which leads to the deterioration of the passivation performance due to suppression of the TiO_x phase transformation [29,30,32].

In this study, we applied HPT to ALD-TiO_x/SiO_y/c-Si heterostructures to improve the performance for ESC as an index of the carrier selectivity (S_{10}). Brendel *et al.* reported that the potential of PCs is evaluated by the following equation [35]:

$$S_{10} = \log_{10} \frac{V_{th}}{J_0 \cdot \rho_c} \qquad (1)$$

where, V_{th}, J_0, and ρ_c denote thermal voltage at 25 °C, the saturation current density, and contact resistivity, respectively. The simultaneous reduction of J_0 and ρ_c is necessary to

improve S_{10} and thus increase the PCE of solar cells. The improvement of the passivation performance reduces J_0 which is related to carrier recombination current. It is reported that J_0 is reduced with the increase of TiO$_x$ thickness. On the other hand, ρ_c is associated with the bulk resistivity of TiO$_x$ and increases with increasing TiO$_x$ thickness. Therefore, TiO$_x$ thickness is a vital factor due to the trade-off relationship between J_0 and ρ_c [27].

In general, even if the materials and deposition methods are limited, the fabrication processes including the chemical solution process before deposition, deposition process, and post-deposition process have many parameters. To prepare TiO$_x$/SiO$_y$/c-Si heterostructures, there are many parameters such as kinds of a chemical solution to form SiO$_y$ interlayers, ALD cycle (C_{ALD}) which determined the TiO$_x$ thickness and HPT parameters: process temperature (T_{HPT}), process time (t_{HPT}), H$_2$ pressure (p_{H_2}), H$_2$ flow rate (R_{H_2}), RF power (P_{RF}) and electrode distance (d). Therefore, the optimization by the comprehensive experiments costs an inordinate amount of time. Recently, materials informatics to integrate machine learning with materials research is developing rapidly. Meanwhile, a few previous works report that machine learning applied to practical experiments of fabrication process (often termed as process informatics) [33,36-39]. Bayesian optimization (BO) is gathering attention as an effective measure to achieve the optimization with a small number of experiments since it can globally optimize the multiple parameters by stochastic prediction [40].

In this research, we applied BO to optimize the fabrication process of ALD-TiO$_x$/SiO$_y$/c-Si heterostructures. The batch process of ALD and HPT was performed onto the three kinds of structure with different pre-deposition treatments to obtain experimental data efficiently. By performing BO for each structure at the same time, we could reveal the superior pre-deposition treatment while optimizing multiple process parameters.

2. Experimental

2.1 Sample preparation

All the TiO_x layers were deposited on double-side-polished, float-zone-grown n-type c-Si(100) substrates by thermal ALD (GEMStar-6, Arradiance). The resistivity and thickness of the substrates were 2.0-4.0 $\Omega \cdot cm$ and 280 ± 20 μm, respectively. Three different kinds of chemical solution processes were performed before the deposition of a TiO_x layer. One set of the substrates were only dipped in 5% HF for 30 seconds (referred to as TiO_x/c-Si hereafter). To insert SiO_y interlayer, after HF dipping, another set of substrates were immersed in 30% hydrogen peroxide (H_2O_2) at room temperature for 10 minutes (referred to as TiO_x/SiO_y(H_2O_2)/c-Si hereafter) and the other set of substrates were immersed in Standard Clean 2 (SC2, 35% hydrochloric acid (HCl): 30% H_2O_2: deionized water = 1:1:4) solution at 60 °C for 10 minutes (referred to as TiO_x/SiO_y(SC2)/c-Si hereafter). Then, TiO_x layers were deposited by ALD at a substrate heater temperature of 150 °C. The metal precursor and oxidant were tetrakis(dimethylamido)titanium and water vapor, respectively. The ALD cycle related to TiO_x layer thickness was changed in a range of 15 to 60 cycles (Table I). After depositing, samples were exposed to the hydrogen plasma produced by a VHF power supply with a frequency of 60 MHz. The electrode area was 138.5 cm^2. There were six variable parameters in HPT: process temperature (T_{HPT}), process time (t_{HPT}), H_2 pressure (p_{H_2}), H_2 flow rate (R_{H_2}), RF power (P_{RF}) and electrode distance (d). Table I shows the empirically determined minimum and maximum values of each parameter.

Table I. Maximum and minimum values of ALD cycle and each parameter of HPT

	C_{ALD} [cycle]	T_{HPT} [°C]	t_{HPT} [min]	p_{H_2} [Pa]	R_{H_2} [sccm]	P_{RF} [W]	d [mm]
Minimum value	15	50	0.25	100	10	270	10
Maximum value	60	300	4	1000	100	420	40

2.2 Characterization

J_0 and the effective carrier lifetime (τ_{eff}) were measured by quasi-steady-state photoconductance decay (QSSPC) using a WCT-120 (Sinton Instruments).

ρ_c was measured by using the Cox-Strack method [41,42]. After HPT, six dots of aluminum (Al)/magnesium (Mg) stack with different diameters in a range of 0.5 to 1.5 mm were deposited on the front side by thermal evaporation. It is noted that the presence of the Mg interlayer plays an important role in reducing the contact resistance without significant degradation of the passivation performance owing to the low workfunction. After removing native oxides on the rear side by HF cleaning, indium gallium (InGa) paste as the electrode was coated on the rear side. For each front electrode dot, current-voltage (I-V) measurement was performed and ρ_c was calculated from the relationship between the resistance and contact area. The details of the Cox-Strack method are given elsewhere [41,42].

The thickness of TiO_x was determined by a spectroscopic ellipsometer (SE, M-2000DI, J. A. Woollam). Previous work revealed that ALD-TiO_x was in the amorphous phase by transmission electron microscopy, thus the Tauc-Lorentz model [43] was used to model the dielectric function of the TiO_x layer [27].

2.3 Bayesian optimization (BO)

BO is an effective measure to globally search the minimum or maximum value of an unknown objective function which has multiple parameters [40]. We used Gaussian process regression (GPR) which can describe the non-linear function and estimate the mean $\mu(x)$ and variance $\sigma^2(x)$ of the posterior probability distribution. The objective function $f(x)$ is modeled as follows:

$$f(x) \approx N(\mu(x), \sigma^2(x)) \qquad (2)$$

where N is the Gaussian distribution. BO can manage the exploration and exploitation in a well-balanced manner by using the prediction uncertainty. The exploration means the searching in the region with large uncertainty which corresponds to the region with few data points. On the other hand, exploitation means searching in the region with a high expected value. An acquisition function determined how the balance between exploration and exploitation. In this work, upper confidence bound (UCB), which expresses the weighted sum of $\mu(x)$ and $\sigma(x)$, was used, as follows:

$$a_{\text{UCB}}(x) \approx \mu(x) + \kappa\sigma(x) \qquad (3)$$

where κ is the user parameter that controls the balance between the exploration and the exploitation. Fig. 1 shows the results of GPR and the states of the optimization by BO. In Fig. 1 (a), the orange line and red circles are the virtual true function and the observations, respectively. Fig. 1 (b) represents the regression result after two observations, and the black dotted line and gray band show $\mu(x)$ and $\sigma(x)$, respectively. It is noted that the band of $\sigma(x)$ becomes narrower around observations because the uncertainty of prediction is

reduced. The value of $a_{\mathrm{UCB}}(x)$ corresponds to the top edge of the gray band. The blue arrows show the conditions to maximize $a_{\mathrm{UCB}}(x)$, which are adopted as the next experimental condition. And then, the prediction model is updated by adding the result at the next experimental condition. Fig. 1 (d) shows that the optimization was performed without being trapped by the localized maximum value ($x \approx 0.2$) due to the uncertainty. And then, in Fig.1 (i), the optimization was achieved. We extended this model to seven-dimensional parameters to optimize the ALD cycle and six variable parameters in HPT.
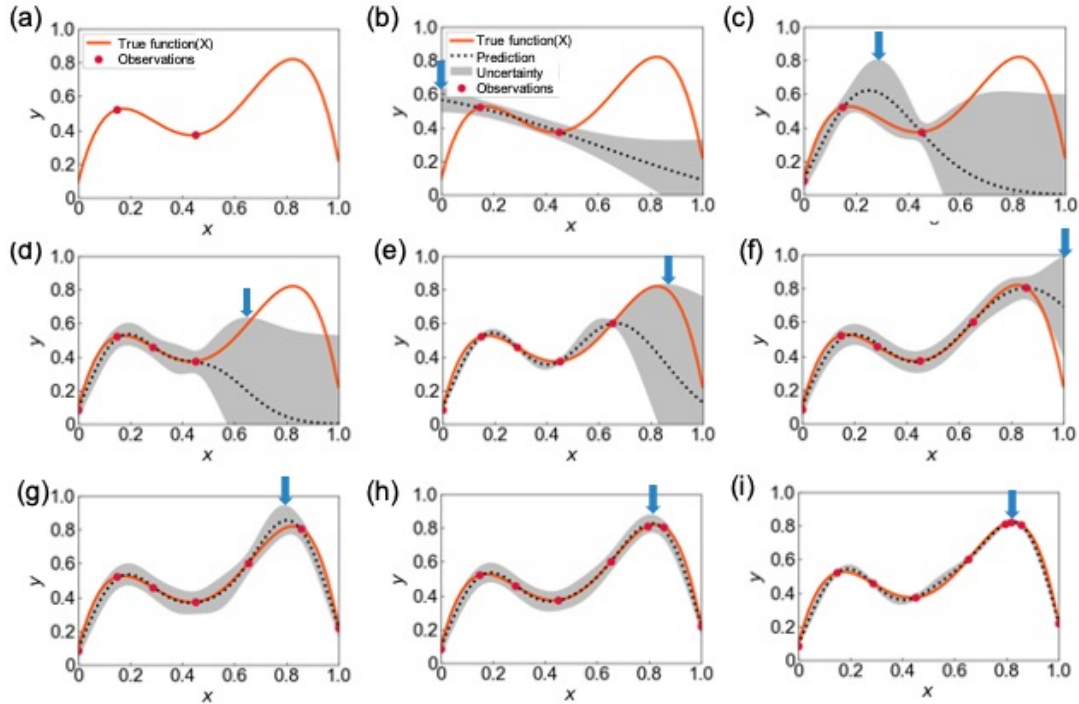
Fig. 1. Results of GPR and state of the optimization by BO based on UCB. The orange line and red circles are the virtual true function and the observations, respectively. The black dotted line and gray band show the expected value curve and the uncertainty of the prediction computed by GPR, respectively. The blue arrows show the maximum value of UCB and the experimental condition that is adopted as the next experimental condition. And then, the prediction model is updated by adding the result at the next experimental condition.

2.4 Cycle of experiments and computations

Fig. 2 shows a schematic of the experimental process and optimization cycle of fabrication of the TiO_x/c-Si, TiO_x/SiO_y(H_2O_2)/c-Si, and TiO_x/SiO_y(SC2)/c-Si heterostructures. Before BO, random ALD cycle and HPT conditions were carried out for 10 samples of each structure in the range of the maximum and minimum values of each parameter (Table I). After HPT, J_0 and ρ_c were measured by QSSPC and Cox-Strack method, respectively. Then S_{10} was calculated from obtained J_0 and ρ_c by eq. (1). It should be remarked that S_{10} neglects the deterioration of the passivation performance by the metallization although we attempted to minimize this effect by employing the Mg interlayer. Those experimental conditions and S_{10} values were set to initial data. Since there are three kinds of structures prepared by different chemical solution processes, a 3-fold number of experiments is required if the parameters are optimized for each structure independently by BO. To obtain the experimental data efficiently, a batch process of ALD and HPT was performed onto the three kinds of structures with different pre-deposition treatments while keeping other experimental conditions the same. After adding the experimental results to the dataset and conducting GPR, UCB values were calculated for each structure. The experimental condition which maximizes UCB value in the three structures was adopted as the next experimental condition. Although this experimental condition is most likely not suitable for improving the performance of other structures, the addition of data will help to expand the search and improve the prediction accuracy of the model. In this way, experiments and computations were sequentially repeated until the experimental condition determined by UCB was unchanged, and thus optimization was completed. By doing this, we can discriminate which pre-deposition treatment is superior while obtaining the optimized condition.
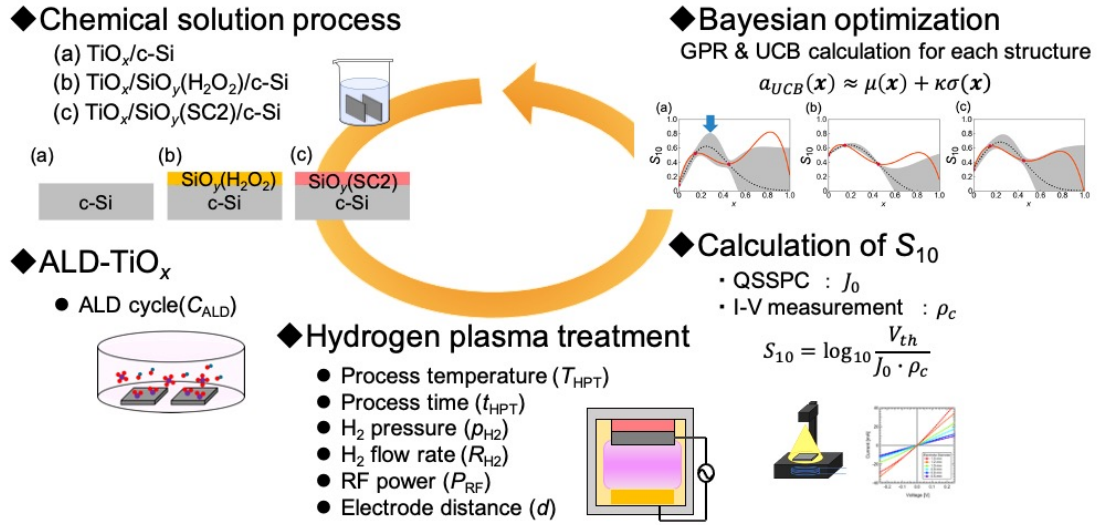
Fig. 2 Schematic of the experimental process and optimization cycle of fabrication of the TiO_x/c-Si, TiO_x/$SiO_y(H_2O_2)$/c-Si, and TiO_x/SiO_y(SC2)/c-Si heterostructures.

3. Experimental results and discussion

Fig. 3 (a) shows the transition of S_{10} of the TiO_x/c-Si, TiO_x/$SiO_y(H_2O_2)$/c-Si and TiO_x/SiO_y(SC2)/c-Si heterostructures. At BO of 12 cycles, the condition determined by UCB was unchanged and thus the optimization is completed. In TiO_x/$SiO_y(H_2O_2)$/c-Si and TiO_x/SiO_y(SC2)/c-Si heterostructures, the high values of S_{10} were obtained when the optimization was achieved at only BO of 12 cycles. In case we use the exhaustive search, there are 234375 different combinations of experimental condition when there are 3 kinds of structures, 7 parameters and 5 levels ($3 \times 5^7 = 234375$). In contrast, the optimization was achieved in a significantly fewer number of experiments by BO. When we used the conventional optimization method based on the principle of local control which fixes all other parameters, it possibly leads to a local maximum or minimum value. Meanwhile, if we assume that the objective function of S_{10}, is the smooth function without singularities in the parameter space of the experimental conditions, we could consider that the global

optimization is achieved by BO.

Fig. 3 (b) shows the transition of the structure which takes the maximum value of UCB, experimental condition, and S_{10} obtained by practical experiment. Hypothetically, when the structure to take the maximum value of UCB remains unchanged for each experiment, the optimization proceeds in only one structure. Then, returned values of the parameters by BO are not optimized values for the others because they may have a higher value than that of the optimized one. However, as shown in Fig. 3(b), the structure which takes the maximum value of UCB changed for each experiment. This result indicates that even in a non-optimized structure the experiments were performed in the batch process under the condition that had not been performed yet and thus the search progressed. Consequently, we can obtain the optimized condition of the superior structure.
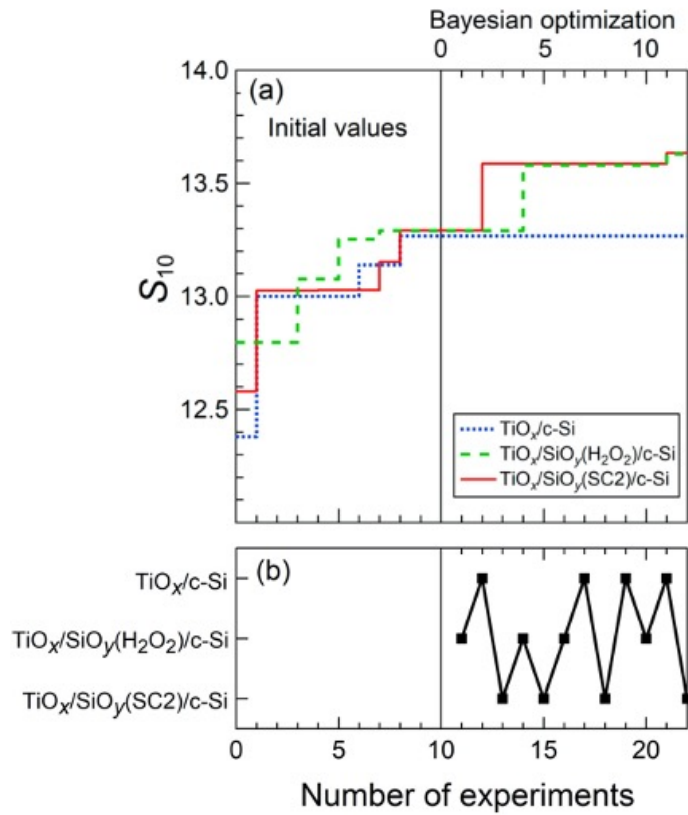
Fig.3 (a) Transition of carrier selectivity S_{10} of the TiO_x/c-Si, TiO_x/SiO_y(H_2O_2)/c-Si and TiO_x/SiO_y(SC2)/c-Si heterostructures. The blue dotted line, the green dashed line and the red solid line represent the TiO_x/c-Si, TiO_x/SiO_y(H_2O_2)/c-Si, and TiO_x/SiO_y(SC2)/c-Si heterostructures, respectively. (b) The transition of the structure which takes the maximum value of UCB, experimental conditions, and S_{10} obtained by practical experiment.

Fig. 4 shows the expected value curved surfaces of the S_{10} of TiO$_x$/SiO$_y$(SC2)/c-Si as a function of T_{HPT} and p_{H_2} at BO of (a) 1, (b) 7 and (c) 12 cycles, respectively. Each figure shows the cross-section from the seven-dimensional space where other parameters were set to the optimized values at that cycle. It is noted that the actual experimental points may not exist on that cross-section because the other parameters are unfixed for each experiment. The expected value curved surface became steeper with the increasing number of cycles, indicating parameters converge on optimized parameter values.

Table II summarizes the optimized conditions and S_{10} values of the TiO$_x$/c-Si, TiO$_x$/SiO$_y$(H$_2$O$_2$)/c-Si, and TiO$_x$/SiO$_y$(SC2)/c-Si heterostructures until BO of 12 cycles. At the optimized condition, the simultaneous reduction of J_0 and ρ_c is achieved. The optimized C_{ALD} of TiO$_x$/SiO$_y$(H$_2$O$_2$)/c-Si and TiO$_x$/SiO$_y$(SC2)/c-Si is 30 cycles and then the thickness of TiO$_x$ measured by SE is 1.97 ± 0.12 nm. This thickness suppresses the increase in the resistance of the TiO$_x$ layer and maintains the high passivation performance and thus obtained high S_{10}.

On the other hand, there are some phenomena related to HPT such as hydrogen radical generation, radical transportation, and radical diffusion into TiO$_x$ as well as plasma damage and crystallization of TiO$_x$. As regards radical generation, radical generation rate G is given as follows:

$$G = k_r N_{H_2} N_e \qquad (4)$$

where k_r, N_{H2} and N_e are reaction rate constant, H$_2$ density, and electron density, respectively. The increase of k_r, N_{H_2}, and N_e leads to increasing G and thus raising the production of the radical. It is needed to increase electron temperature for larger k_r. Lower

p_{H_2} or lower d leads to raising electron temperature. On the other hand, increasing p_{H_2} and R_{H_2} needs to increase N_{H_2}. As for N_e, larger P_{RF} leads to increase of N_e. In terms of radical transportation, it is necessary to consider p_{H_2} and R_{H_2} in order to form a uniform plasma. When p_{H_2} is too high, the amount of radical incident on the TiO$_x$ surface may decrease because of the short free-path length of the radical. Meanwhile, as for R_{H_2} lower value causes unstable plasma, whereas a higher value induces turbulence. Regarding radical diffusion into TiO$_x$, it is necessary to consider T_{HPT} for sufficient diffusion to heterointerface. It was reported that hydrogen easily diffuses into crystalline TiO$_x$ films at 200 °C [44] and it is consistent with this research. Moreover, sufficient t_{HPT} is needed for the adequate supply of radical to heterointerface which is necessary for enhancing the passivation performance. Regarding plasma damage, it is needed to consider the ion bombardment and light soaking. It was reported that an increase of the a-Si:H/c-Si interface defect density was observed after plasma processing [45] and lower P_{RF} or higher p_{H_2} are needed to decrease the ion bombardment [46]. Moreover, it was reported that the performance of solar cells using TiO$_x$ deteriorates during light soaking [34]. Therefore, it is desired short t_{HPT} to reduce plasma damage. In terms of crystallization of TiO$_x$, lower T_{HPT} and short t_{HPT} are needed to suppress the crystallization of TiO$_x$ which causes the deterioration of the passivation performance. As above, these phenomena are complexly intertwined via six HPT parameters. Therefore, it is hard to find the optimized conditions by conventional methods. Although optimization can be done based on expert experience and hypothesis, the optimized parameters are likely to be local maximum or minimum. Meanwhile, BO globally optimized the HPT parameters and thus the optimized S_{10} could be the global maximum within determined parameter dimensions.
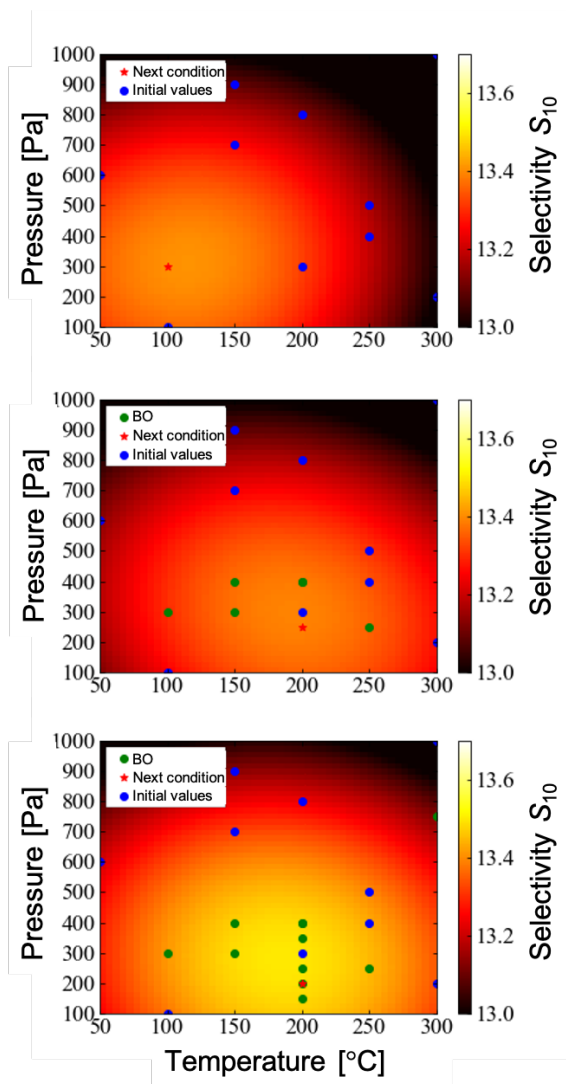
Fig.4 The expected value curved surfaces of the S_{10} of TiO_x/SiO_y(SC2)/c-Si as a function of process temperature and H_2 pressure at BO of (a) 1, (b) 7 and (c) 12 cycles, respectively.

Table II The conditions which obtained the highest S_{10} and S_{10} values of the TiO_x/c-Si, TiO_x/SiO_y(H_2O_2)/c-Si, and TiO_x/SiO_y(SC2)/c-Si heterostructures until BO of 12 cycles.

Structure	C_{ALD}	T_{HPT}	t_{HPT}	p_{H_2}	R_{H_2}	P_{RF}	d	S_{10}
	[cycle]	[°C]	[min]	[Pa]	[sccm]	[W]	[mm]	[-]
TiO_x/c-Si	15	100	0.75	100	70	390	10	13.27
TiO_x/SiO_y(H_2O_2)/c-Si	30	200	1.5	200	70	300	20	13.63
TiO_x/SiO_y(SC2)/c-Si	30	200	1.5	200	70	300	20	13.63

Table III The S_{eff} (at MCD of 1×10^{15} cm^{-3}), J_0 (at MCD of 5×10^{15} cm^{-3}), ρ_c, S_{10} and $\eta_{theoretical}$ of TiO_x/c-Si, TiO_x/SiO_y(H_2O_2)/c-Si and TiO_x/SiO_y(SC2)/c-Si heterostructures at the condition which obtained the highest S_{10}.

Structure	S_{eff}	J_0	ρ_C	S_{10}	$S_{10}{}^*$
	[cm/s]	[fA/cm^2]	[$\Omega \cdot cm^2$]	[-]	[-]
TiO_x/c-Si	20.3	33.3	0.0410	13.27	12.85
TiO_x/SiO_y(H_2O_2)/c-Si	10.0	18.5	0.0320	13.63	13.21
TiO_x/SiO_y(SC2)/c-Si	11.5	20.7	0.0286	13.63	13.21

It should be remarked that the optimized S_{10} does not include the deterioration of the passivation performance by the metallization. In order to estimate this effect, we prepared asymmetric samples passivated with a-Si:H at the front side and the stack of TiO_x/SiO_y at the rear side. Photoluminescence images were taken before and after the full metallization of the rear side by Al with the Mg interlayer. From the reduction of PL intensity, the increase in J_0 by the metallization was estimated as a factor of 2.6. If we apply this factor,

we could estimate $S_{10}{}^{*}$ including the impact of the metallization.

Table III shows the effective surface recombination velocity (S_{eff}), J_0, ρ_c, S_{10}, and $S_{10}{}^{*}$ of the TiO$_x$/c-Si, the TiO$_x$/SiO$_y$(H$_2$O$_2$)/c-Si, and the TiO$_x$/SiO$_y$(SC2)/c-Si heterostructures at the condition which obtained the highest S_{10}. The J_0 values were extracted at minority carrier density (MCD) of 5×10^{15} cm^{-3}. S_{eff} of symmetrically coated c-Si is defined as follows:

$$\frac{1}{\tau_{\mathrm{eff}}} = \frac{1}{\tau_{\mathrm{bulk}}} + \frac{2S_{\mathrm{eff}}}{W} \qquad (5)$$

where, τ_{bulk} and W are bulk Si lifetime and wafer thickness of 280 μm, respectively. Here the τ_{bulk} is assumed to be infinite in the calculation since high-quality Si substrates were used. The τ_{eff} at an excess MCD of 1.0×10^{15} cm^{-3} was used to calculate S_{eff}.

J_0 is defined as follows:

$$\frac{1}{\tau_{\mathrm{eff}}} - \frac{1}{\tau_{\mathrm{Auger}}} = \frac{1}{\tau_{\mathrm{bulk}}} + 2J_0\frac{n}{qn_{\mathrm{i}}{}^2W} \qquad (6)$$

where, τ_{Auger}, q, n_{i}, and n are Auger lifetime, elementary charge, intrinsic carrier density, and excess MCD, respectively. When $1/\tau_{\mathrm{eff}} - 1/\tau_{\mathrm{Auger}}$ is plotted versus n, a straight-line results which have a slope proportional to J_0 [47].

Fig. 5 shows $1/\tau_{\mathrm{eff}} - 1/\tau_{\mathrm{Auger}}$ of as-deposited and optimized condition performed each structure as a function of excess MCD. In all of the structures, the J_0 at excess MCD of 5 $\times$ 10^{15} was decreased by HPT. In previous work, hydrogen radicals formed by HPT diffuses to TiO$_x$/c-Si and terminates the dangling bonds and thus the chemical passivation

improves [32]. Besides, when TiO$_x$ is partially reduced, the number of oxygen vacancy increases, and then free electrons are generated [31]. This rise of the electron density leads to the large band bending at TiO$_x$/c-Si heterointerface, which can improve field effect passivation and electron selectivity. Compared with the TiO$_x$/c-Si heterostructure, low J_0 values are observed for the TiO$_x$/SiO$_y$(H$_2$O$_2$)/c-Si and the TiO$_x$/SiO$_y$(SC2)/c-Si heterostructures. This results from Si-O-Ti bonding by inserting SiO$_y$ interlayer which enhances the diffusion of Ti and O atoms from TiO$_x$ to SiO$_y$. The difference of J_0 between the TiO$_x$/SiO$_y$(H$_2$O$_2$)/c-Si and the TiO$_x$/SiO$_y$(SC2)/c-Si heterostructures is probably caused by the film density of SiO$_y$ interlayer depends on chemicals. In terms of S_{10}, however, both of them take almost the same value, indicating that carrier selectivity is not mainly dominated by the structure of the SiO$_y$ interlayers but also by HPT condition.

Fig. 6 shows the difference between total resistance (R_T) and spreading resistance (R_S) as a function of contact area (S). The ρ_c is defined as follows:

$$R_{\mathrm{T}} - R_{\mathrm{S}} = \frac{\rho_c}{S} + R_0 \qquad (7)$$

where R_0 is residual resistance. The relatively low ρ_c values of the TiO$_x$/SiO$_y$(H$_2$O$_2$)/c-Si and the TiO$_x$/SiO$_y$(SC2)/c-Si heterostructures can be achieved. These results indicate Fermi-level depinning thanks to their high passivation performance. On the other hand, the ρ_c value of TiO$_x$/c-Si is high due to the Fermi energy pinning which is known to be pinned at the defect level at the heterointerfaces.

The $\eta_{\mathrm{theoretical}}$ is calculated by the equation as follows [35]:

$$\eta_{\text{theoretical}} = ((2.452\, S_{10} - 4.240)^{-19.52} + (29.21)^{-19.52})^{-\frac{1}{19.52}}. \qquad (8)$$

In the $TiO_x/SiO_y(H_2O_2)$/c-Si and the TiO_x/SiO_y(SC2)/c-Si heterostructures, the highest $\eta_{\text{theoretical}}$ of 27.59% was obtained by using $S_{10}{}^*$. In addition, low thermal budget thanks to short process time and low process temperature suppresses causing phase transformation and crystallization of TiO_x. Therefore, this fabrication process of TiO_x/SiO_y/c-Si heterostructure is desirable to apply SHJ solar cells and the high PCE could be expected.
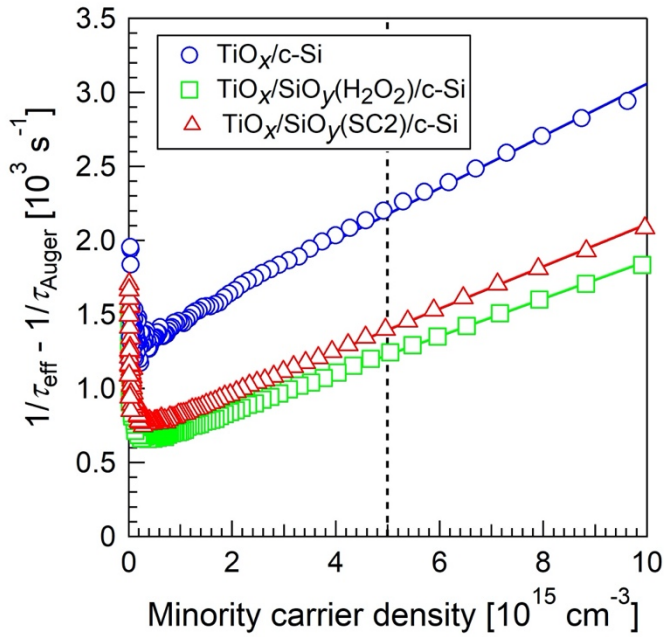

Fig. 5 The $1/\tau_{\text{eff}} - 1/\tau_{\text{Auger}}$ of as-deposited and after optimized HPT of (a) TiO_x/c-Si, (b) $TiO_x/SiO_y(H_2O_2)$/c-Si and (c) TiO_x/SiO_y(SC2)/c-Si heterostructures as a function of excess minority carrier density.
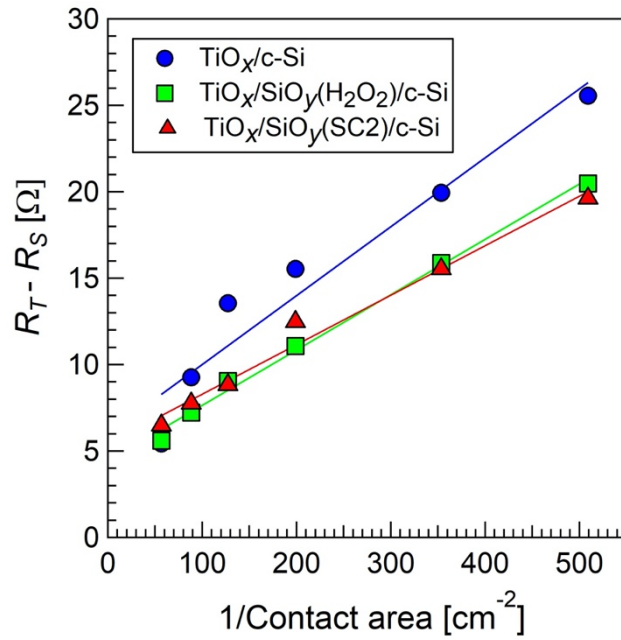
Fig. 6 The difference between total resistance (R_T) and spreading resistance (R_S) of TiO$_x$/c-Si, TiO$_x$/SiO$_y$(H$_2$O$_2$)/c-Si, and TiO$_x$/SiO$_y$(SC2)/c-Si heterostructures performed optimized process as a function of contact area (S).

4. Conclusion

We applied BO to optimize the fabrication process of the ALD-TiO$_x$/SiO$_y$/c-Si heterostructure to improve the performance for passivating contacts. We attempted to optimize three kinds of chemical solution before deposition of TiO$_x$, ALD cycle, and HPT parameters: process temperature, process time, H$_2$ pressure, H$_2$ flow rate, RF power and electrode distance. At BO of 12 cycles, the condition determined by UCB was unchanged and thus the optimization is achieved. Although we need to consider the deterioration of the passivation by the metallization, we could conclude that BO is useful to optimize the experimental conditions which has multidimensional parameter space. Fine tuning of the conditions starting with the optimized conditions by BO, we could expect realization of high efficiency SHJ solar cells utilizing TiO$_x$.

Data Availability

  The data that support the findings of this study are available from the corresponding author upon reasonable request.

Reference

[1] K. Masuko, M. Shigematsu, T. Hashiguchi, D. Fujishima, M. Kai, N. Yoshimura, T. Yamaguchi, Y. Ichihashi, T. Mishima, N. Matsubara, T. Yamanishi, T. Takahama, M. Taguchi, E. Maruyama, S. Okamoto, Achievement of more than 25% conversion efficiency with crystalline silicon heterojunction solar cell, IEEE J. Photovoltaics **4** (2014) 1433-1435. https://doi.org/ 10.1109/JPHOTOV.2014.2352151

[2] M. Taguchi, A. Yano, S. Tohoda, K. Matsuyama, Y. Nakamura, T. Nishiwaki, K. Fujita, E. Maruyama, 24.7% record efficiency HIT solar cell on thin silicon wafer, IEEE J. Photovoltaics **4** (2014) 96–99. https://doi.org/10.1016/j.egypro.2015.07.072

[3] D. Adachi, J.L. Hernandez, K. Yamamoto, Impact of carrier recombination on fill factor for large area heterojunction crystalline silicon solar cell with 25.1% efficiency, Appl. Phys. Lett. **107** (2015) 233506. https://doi.org/10.1063/1.4937224

[4] K.Yoshikawa, H.Kawasaki, W.Yoshida, K.Konishi, K.Nakano, T.Uno, D.Adachi, M. Kanematsu, H. Uzu, K. Yamamoto, Silicon heterojunction solar cell with interdigitated back contacts for a photoconversion efficiency over 26%, Nat. Energy **2** (2017) 17032. https://doi.org/10.1038/nenergy.2017.32

[5] A.A. Langford, M.L. Fleet, B.P. Nelson, Infrared absorption strength and hydrogen content of hydrogenated amorphous silicon, Phys. Rev. B **45** (1992) 13367-13377. https://doi.org/10.1103/PhysRevB.45.13367

[6] A.S. Ferlauto, G.M. Ferreira, J.M. Pearce, C.R. Wronski, R.W. Collins, X. Deng, G. Ganguly, Analytical model for the optical functions of amorphous semiconductors from the near-infrared to ultraviolet: applications in thin film photovoltaics, J. Appl. Phys. **92** (2002) 2424-2436. https://doi.org/10.1063/1.1497462

[7] Z.C. Holman, A. Descoeudres, L. Barraud, F.Z. Fernandez, J.P. Seif, S. De Wolf, C.

Ballif, Current losses at the front of silicon heterojunction solar cells, IEEE J. Photovoltaics **2** (2012) 7–15. https://doi.org/10.1109/JPHOTOV.2011.2174967

[8] L.G. Gerling, S. Mahato, A. Morales-Vilches, G. Masmitja, P. Ortega, C. Voz, R. Alcubilla, J. Puigdollers, Transition metal oxides as hole-selective contacts in silicon heterojunctions solar cells, Sol. Energy Mater. Sol. Cells **145** (2016) 109–115. https://doi.org/10.1016/j.solmat.2015.08.028

[9] C. Battaglia, S.M. de Nicolas, S. De Wolf, X. Yin, M. Zheng, C. Ballif, A. Javey, Silicon heterojunction solar cell with passivated hole selective MoO_x contact, Appl. Phys. Lett. **104** (2014) 113902. https://doi.org/10.1063/1.4868880

[10] J. Geissbühle, J. Werner, S.M. Nicolas, L. Barraud, A. Hessler-Wyser, M. Despeisse, S. Nicolay, A. Tomasi, B. Niesen, S. De Wolf, C. Ballif, 22.5% efficient silicon heterojunction solar cell with molybdenum oxide hole collector, Appl. Phys. Lett. **107** (2015) 081601. https://doi.org/10.1063/1.4928747

[11] J. Dréon, Q. Jeangros, J. Cattin, J. Haschke, L. Antognini, C. eBallif, M. Boccard, 23.5%-efficient silicon heterojunction silicon solar cell using molybdenum oxide as hole-selective contact, Nano Energy **70** (2020) 104495. https://doi.org/10.1016/j.nanoen.2020.104495

[12] G. Masmitj, L.G. Gerling, P. Ortega, J. Puigdollers, I. Martin, C. Voz, R. Alcubilla, V_2O_x-based hole-selective contacts for c-Si interdigitated back-contacted solar cells, J. Mater. Chem. **5** (2017) 9182–9189. https://doi.org/10.1039/C7TA01959A

[13] M.Mews, A.Lemaire, L.Korte, Sputtered tungsten oxide as hole contact for silicon heterojunction solar cells, IEEE J. Photovoltaics **7** (2017) 1209–1215. https://doi.org/10.1109/JPHOTOV.2017.2714193

[14] S. Avasthi, W.E. McClain, G. Man, A. Kahn, J. Schwar, J.C. Strum, Hole-blocking

titanium-oxide/silicon heterojunction and its application to photovoltaics, Appl. Phys. Lett. **102** (2013) 203901. https://doi.org/10.1063/1.4803446

[15] X. Yang, P. Zheng, Q. Bi, K. Weber, Silicon heterojunction solar cells with electron selective TiO_x contact, Sol. Energy Mater. Sol. Cells **150** (2016) 32–38. https://doi.org/10.1016/j.solmat.2016.01.020

[16] X. Yang, Q. Bi, H. Ali, K. Davis, W.V. Schoenfeld, K. Weber, High-performance TiO_2-based electron-selective contacts for crystalline silicon solar cells, Adv. Mater. **28** (2016) 5891–5897. https://doi.org/10.1002/adma.201600926

[17] X. Yang, K. Weber, Z. Hameiri, S.D. Wolf, Industrially feasible, dopant-free, carrier-selective contacts for high-efficiency silicon solar cells, Prog. Photovoltaics Res. Appl. **25** (2017) 896–904. https://doi.org/10.1002/pip.2901

[18] K.A. Nagamatsu, S. Avasthi, G. Sahasrabudhe, G. Man, J. Jhaveri, A.H. Berg, J. Schwartz, A. Kahn, S. Wagner, J.C. Strum, Titanium dioxide/silicon hole- blocking selective contact to enable double-heterojunction crystalline silicon-based solar cell, Appl. Phys. Lett. **106** (2015) 123906. https://doi.org/10.1063/1.4916540

[19] D. O. Scanlon, C. W. Dunnill, J. Buckeridge, S. A. Shevlin, A. J. Logsdail, S. M. Woodley, C. R. A. Catlow, M. J. Powell, R. G. Palgrave, I. P. Parkin, G. W. Watson, T. W. Keal, P. Sherwood, A. Walsh, A. A. Sokol, Band alignment of rutile and anatase TiO_2. Nature Mater **12** (2013) 798–801. https://doi.org/10.1038/nmat3697

[20] J. Aarik, A. Aidla, A. Kiisler, T. Uustare, V. Sammelselg, Effect of crystal structure on optical properties of TiO_2 films grown by atomic layer deposition, Thin Solid Films **305** (1997) 270–273. https://doi.org/10.1016/S0040-6090(97)00135-1

[21] J. Bullock, Y. Wan, Z. Xu, S. Essig, M. Hettick, H. Wang, W. Ji, M. Boccard, A. Cuevas, C. Ballif, A. Javey, Stable dopant-free asymmetric heterocontact silicon solar

cells with efficiencies above 20%, ACS Energy Lett **3** (2018) 508–513. https://doi.org/10.1021/acsenergylett.7b01279

[22] B. Liao, B. Hoex, A.G. Aberle, D. Chi, C.S. Bhatia, Excellent c-Si surface passivation by low-temperature atomic layer deposited titanium oxide, Appl. Phys. Lett. **104** (2014) 253903. https://doi.org/10.1063/1.4885096

[23] B. Liao, B. Hoex, K.D. Shetty, P.K. Basu, C.S. Bhatia, Passivation of boron-doped industrial silicon emitters by thermal atomic layer deposited titanium oxide, IEEE J. Photovoltaics **5** (2015) 1062–1066. https://doi.org/10.1109/JPHOTOV.2015.2434596

[24] K.M. Gad, D. Vossing, A. Richter, B. Rayner, L.M. Reindl, S.E. Mohney, M. Kasemann, Ultrathin titanium dioxide nanolayers by atomic layer deposition for surface passivation of crystalline silicon, IEEE J. Photovoltaics **6** (2016) 649–653. https://doi.org/10.1109/JPHOTOV.2016.2545404

[25] M.M. Plakhotnyuk, N. Schuler, E. Shkodin, R.A. Vijayan, S. Masilamani, M. Varadharajaperumal, A. Crovetto, O. Hansen, Surface passivation and carrier selectivity of the thermal-atomic-layer-deposited TiO_2 on crystalline silicon, Jpn. J. Appl. Phys. **56** (2017) 08MA18. https://doi.org/10.7567/JJAP.56.08MA11

[26] V. Titova, B. Veith-Wolf, D. Startsev, J. Schmidt, Effective passivation of crystalline silicon surfaces by ultrathin atomic-layer-deposited TiO_x layers, Energy Procedia **124** (2017) 441–447. https://doi.org/10.1016/j.egypro.2017.09.272

[27] T. Mochizuki, K. Gotoh, Y. Kurokawa, T. Yamamoto, N. Usami, Local structure of high performance TiOx electron-selective contact revealed by electron energy loss spectroscopy, Adv. Mater. Interfaces **6** (2018) 1801645. https://doi.org/10.1002/admi.201801645

[28] K. Gotoh, T. Mochizuki, T. Hojo, Y. Shibayama, Y. Kurokawa, E. Akiyama, N.

Usami, Activation energy of hydrogen desorption from high-performance titanium oxide carrier-selective contacts with silicon oxide interlayers, Curr. Appl Phys. **21**, (2021) 36-42. https://doi.org/10.1016/j.cap.2020.10.002

[29] Mochizuki, K. Gotoh, A. Ohta, S. Ogura, Y. Kurokawa, S. Miyazaki, K. Fukutani, N. Usami, Activation mechanism of TiO_x passivating layer on crystalline Si, Appl. Phys. Express **11** (2018) 102301. https://doi.org/10.7567/APEX.11.102301

[30] Y. Nakagawa, K. Gotoh, M. Wilde, S. Ogura, Y. Kurokawa, K. Fukutani, N. Usami, Effect of forming gas annealing on hydrogen content and surface morphology of titanium oxide coated crystalline silicon heterocontacts, J. Vac. Sci. Technol. A **38** (2020) 022415. https://doi.org/10.1116/1.5134719

[31] S. Bhatia, I. M. Khorakiwala, P. R. Nair, Aldrin Antony, Room temperature H_2 plasma treatment for enhanced passivation of silicon/TiO_2 interface, Appl. Phys. Lett. **113** (2018) 171603.   https://doi.org/10.1063/1.5035459

[32] S. Miyagawa, K. Gotoh, S. Ogura, M. Wilde, Y. Kurokawa, K. Fukutani, N. Usami, Effect of hydrogen plasma treatment on the passivation performance of TiO_x on crystalline silicon prepared by atomic layer deposition, J. Vac. Sci. Technol. A **38** (2020) 022410. https://doi.org/10.1116/1.5134720

[33] S. Miyagawa, K. Gotoh, K. Kutsukake, Y. Kurokawa, N. Usami, Application of Bayesian optimization for improved passivation performance in TiO_x/SiO_y/c-Si heterostructure by hydrogen plasma treatment, Appl. Phys. Express **14** (2021) 025503. https://doi.org/10.35848/1882-0786/abd869

[34] T. Matsui, M. Bivour, M. Hermle, H. Sai, Atomic-Layer-Deposited TiO_x Nanolayers Function as Efficient Hole-Selective Passivating Contacts in Silicon Solar Cells, ACS Appl.   Mater.   Interfaces   **12**   (2020)   49777-49785.

https://dx.doi.org/10.1021/acsami.0c14239

[35] R. Brendel, R. Peidst, Contact selectivity and efficiency in crystalline silicon photovoltaics, IEEE J. Photovoltaics **6** (2016) 1413–1420. https://dx.doi.org/10.1109/JPHOTOV.2016.2598267

[36] D. Xue, P. V. Balachandran, J. Hogden, J. Theiler, D. Xue, T. Lookman, Accelerated search for materials with targeted properties by adaptive design, Nat. Commun. **7** (2016) 11241. https://doi.org/10.1038/ncomms11241

[37] S. Subianto, C. Li, D. Rubin De Celis Leal, S. Rana, S. Gupta, R. He, S. Venkatesh, A. Sutti, Optimizing a High-Entropy System: Software-Assisted Development of Highly Hydrophobic Surfaces using an Amphiphilic Polymer, ACS Omega **4** (2019) 15912. https://doi.org/10.1021/acsomega.9b01978

[38] Y. K. Wakabayashi, T. Otsuka, Y. Krockenberger, H. Sawada, Y. Taniyasu, H. Yamamoto, Machine-learning-assisted thin-film growth: Bayesian optimization in molecular beam epitaxy of $SrRuO_3$ thin films, APL Mater. **7** (2019) 101114. https://doi.org/10.1063/1.5123019

[39] K. Osada, K. Kutsukake, J. Yamamoto, S. Yamashita, T. Kodera, Y. Nagai, T. Horikawa, K. Matsui, I. Takeuchi, T. Ujihara, Adaptive Bayesian optimization for epitaxial growth of Si thin films under various constraints, Mater. Today Commun. **25** (2020) 101538. https://doi.org/10.1016/j.mtcomm.2020.101538

[40] B. Shahriari, K. Swersky, Z. Wang, R. P. Adams, N. De Freitas, Taking the Human Out of the Loop: A Review of Bayesian Optimization, Proc. IEEE **104** (2016) 148-175. https://doi.org/10.1109/JPROC.2015.2494218

[41] R. Cox, H. Strack, Ohmic contacts for GaAs devices, Solid State Electron. **10** (1967) 1213–1218. https://doi.org/10.1016/0038-1101(67)90063-9

[42] W. Wang, H. Lin, Z. Yang, Z. Wang, J. Wang, L. Zhang, M. Liao, Y. Zeng, P. Gao, B. Yan, J. Ye, An expanded Cox and Strack method for precise extraction of specific contact resistance of transition metal oxide/n-silicon heterojunction, IEEE Photovolt **9** (2019) 1113–1120. https://doi.org/10.1109/JPHOTOV.2019.2917386

[43] G.E. Jellison Jr., F.A. Modine, Parameterization of the optical functions of amorphous materials in the interband region, Appl. Phys. Lett. **69** (1996) 371–373. https://doi.org/10.1063/1.118064

[44] A. Sasinska, T. Singh, S. Wang, S. Mathur, and R. Kraehnert, Enhanced photocatalytic performance in atomic layer deposition grown TiO2 thin films via hydrogen plasma treatment, J. Vac. Sci. Technol. A **33** (2015) A152. https://doi.org/10.1116/1.4904503

[45] J. Geissbühler, S. De Wolf, B. Demaurex, J. P. Seif, D. T. L. Alexander, L. Barraud, and C. Ballif, Amorphous/crystalline silicon interface defects induced by hydrogen plasma treatments, Appl. Phys. Lett. **102** (2013) 231604. https://doi.org/10.1063/1.4811253

[46] M. Mews, E. Conrad, S. Kirner, N. Mingirulli, and L. Korte, Hydrogen Plasma Treatments of Amorphous/Crystalline Silicon Heterojunctions, Energy Procedia **55** (2014) 827-833. https://doi.org/10.1016/j.egypro.2014.08.066

[47] R. R. King, R. A. Sinton and R. M. Swanson, Studies of diffused phosphorus emitters: saturation current, surface recombination velocity, and quantum efficiency, IEEE Trans. Electron Devices **37** (1990) 365-371. https://doi.org/10.1109/16.46368.